

openings with aperture angles of 98°. This geometry allows us to probe acoustic phonons propagating in any direction parallel to diamond faces. Brillouin measurements at a scattering geometry of 90° (angle accuracy, 0.5°) were made in 10° intervals of rotation angle ϕ in the laboratory frame, namely, the rotation of DAC about the load axis with an uncertainty of $\pm 0.2^\circ$. The observed Brillouin frequency shifts, that is, sound velocities at 1.50 GPa, are plotted as a function of ϕ as open circles in Fig. 2.

To analyze the angular dependence of acoustic velocities of the longitudinal (LA) and two transverse, slow (TA₁) and fast (TA₂), modes at each applied pressure, it is necessary to use the usual Brillouin equation and Every's closed-form expressions (16) relating sound velocities for arbitrary directions to the elastic constants. We can easily modify Every's velocity expressions for cubic crystals to our experimental system by using the Euler angles, instead of the direction cosines of \mathbf{q} in the crystal axis frame. The velocities can therefore be expressed as a function of six parameters: $v_i^2 = f(C_{11}/\rho, C_{12}/\rho, C_{44}/\rho, \theta, \phi, \chi)$, where the subscript i indicates LA, TA₁, and TA₂ modes. A computerized least-squares fit was applied to determine elastic properties of the fcc H₂S crystal at each pressure. There is excellent agreement between the measured and the fitted values, because each elastic constant depends anisotropically or dominantly on its special directions. The best fitting results yielded $C_{11}/\rho = 98.0$, $C_{12}/\rho = 72.9$, and $C_{44}/\rho = 43.4$ kbar · cm³/g at 1.50 GPa. An independent procedure for different crystal orientations showed excellent consistency for these values within an accuracy of $\pm 2\%$.

The pressure dependences of the crystal orientation and elastic properties were determined by the best fit to the angular dependence of sound velocities under each applied pressure. The single crystal orientation changed in the DAC by the increasing uniaxial stress component with pressure: (θ, ϕ, χ); (76.4; 6.8, 21.2), (77.0, 7.1, 19.8), and (79.2, 11.0, 17.7) at pressures of 3.69, 4.58, and 6.12 GPa, respectively, where the measurements were made on the same point of the H₂S crystal. These data indicate that it is necessary to make in situ determinations of both the crystal orientation and the elastic properties at each applied pressure in order to study condensed gases in the DAC. From the set of six parameters obtained, the sound velocities could be calculated for all directions of each crystal orientation (see Fig. 3 for typical directions). Furthermore, we can calculate the acoustic velocities (v_{180}) along the Z direction (load axis) in the laboratory frame, which are available to determine n as follows: At backscattering geometry (180°) the Brillouin frequency shift ($\Delta\nu_{180}$) is related to v_{180} by the expression

$$v_{180} = \Delta\nu_{180} \cdot \frac{\lambda_0}{(2n)} \quad (2)$$

By using the measured $\Delta\nu_{180}$ and the calculated v_{180} by the best fitting method, we could estimate n from Eq. 2 at each applied pressure (Fig. 4A). The value of n is 1.69 at 1.50 GPa and increases with pressure up to 1.98 at 7.0 GPa. From these results, the Lorentz-Lorenz relation $(n^2 - 1)/(n^2 + 2) = 4\pi N\rho\alpha/3M$ yields ρ as a function of pressure (Fig. 4B), that is, the EOS, where N is Avogadro's number, M is the molecular weight, and α is polarizability with a value of 3.78×10^{-24} cm³ (17), which is assumed to be pressure-insensitive (18). The density, ρ , is 1.37 g/cm³ at 1.50 GPa and increases with pressure up to 1.78 g/cm³ at 7.0 GPa (19). For the present method, the error is within $\Delta\rho/\rho = \pm 3.8\%$ for $n = 1.7$, where the uncertainties in the measured frequency shift and in the determined refractive index are about $\Delta(\Delta\nu)/\Delta\nu = \pm 1\%$ and $\Delta n/n = \pm 2\%$, respectively.

Finally, on the basis of the pressure dependence of ρ , the elastic constants C_{11} , C_{12} , and C_{44} were determined as a function of pressure (Fig. 4C). The elastic anisotropy $A = 2C_{44}/(C_{11} - C_{12})$ is calculated to be 3.45 at 1.50 GPa. This is close to the value of 3.60 for fcc plastic crystal CH₄ at 1 bar and 90 K (20).

High-pressure Brillouin spectroscopy provides a new approach for the study of elastic properties of condensed gases in the DAC under ultrahigh pressures. It will be worthwhile to apply this new method to the fcc and hexagonal close-packed systems for simple condensed gases under ultrahigh pressures.

REFERENCES AND NOTES

1. H. Shimizu, E. M. Brody, H. K. Mao, P. M. Bell, *Phys. Rev. Lett.* **47**, 128 (1981).

2. A. Jayaraman, *Rev. Mod. Phys.* **55**, 65 (1983).
3. R. J. Hemley, P. M. Bell, H. K. Mao, *Science* **237**, 605 (1987).
4. M. Grimsditch and A. Polian, in *Simple Molecular Systems at Very High Density*, A. Polian, P. Loubeyre, N. Boccardo, Eds. (Plenum, New York, 1989), pp. 237–255.
5. H. Shimizu, T. Kumazawa, E. M. Brody, H. K. Mao, P. M. Bell, *Jpn. J. Appl. Phys.* **22**, 52 (1983).
6. A. Polian and M. Grimsditch, *Phys. Rev. Lett.* **52**, 1312 (1984).
7. S. A. Lee, D. A. Pinnick, S. M. Lindsay, R. C. Hanson, *Phys. Rev. B* **34**, 2799 (1986).
8. M. Gauthier, Ph. Pruzan, J. C. Chervin, A. Polian, *Solid State Commun.* **68**, 149 (1988).
9. J. van Straaten and I. F. Silvera, *Phys. Rev. B* **37**, 1989 (1988).
10. H. K. Mao *et al.*, *Science* **239**, 1131 (1988).
11. R. J. Hemley *et al.*, *Phys. Rev. B* **42**, 6458 (1990).
12. E. Sandor and S. O. Ogunade, *Nature* **224**, 905 (1969).
13. H. Shimizu, Y. Nakamichi, S. Sasaki, *J. Chem. Phys.* **95**, 2036 (1991).
14. ———, in *Molecular Systems Under High Pressure*, R. Pucci and G. Piccitto, Eds. (Elsevier, Amsterdam, 1991), pp. 273–281.
15. C. H. Whitfield, E. M. Brody, W. A. Bassett, *Rev. Sci. Instrum.* **47**, 942 (1976).
16. A. G. Every, *Phys. Rev. Lett.* **42**, 1065 (1979).
17. J. O. Hirschfelder, C. F. Curtiss, R. B. Bird, *Molecular Theory of Gases and Liquids* (Wiley, New York, 1963).
18. Because H₂S molecules exist in a nearly homogeneous field of the plastic (OD) phase, this assumption is reasonable.
19. The thermodynamic relation,

$$\rho(P_B) - \rho(P_A) = \int_{P_A}^{P_B} (\gamma_s/v_s^2) dP$$

where P is pressure, also gives us an estimate of the EOS (1–4), where $\gamma_s = C_p/C_v$ is the ratio of the specific heats at constant pressure to constant volume, and $v_s^2 = (C_{11}/\rho + 2C_{12}/\rho)/3$ for the cubic system. By using the present EOS determined from the Lorentz-Lorenz relation and the pressure dependence of v_s^2 , we could estimate the reasonable pressure dependence of γ_s : $\gamma_s = 1.1$ at 0.5 GPa and decreases to 1.0 at pressures above 2 GPa.

20. S. C. Rand and B. P. Stoicheff, *Can. J. Phys.* **60**, 287 (1982).

11 February 1992; accepted 7 May 1992

Evidence for Liquid-Phase Cirrus Cloud Formation from Volcanic Aerosols: Climatic Implications

Kenneth Sassen

Supercooled droplets in cirrus uncinus cell heads between -40° and -50°C are identified from Project FIRE [First ISCCP (International Satellite Cloud Climatology Project) Regional Experiment] polarization lidar measurements. Although short-lived, complexes of these small liquid cells seem to have contributed importantly to the formation of the cirrus. Freezing-point depression effects in solution droplets, apparently resulting from relatively large cloud condensation nuclei of volcanic origin, can be used to explain this rare phenomenon. An unrecognized volcano-cirrus cloud climate feedback mechanism is implied by these findings.

Pilots and scientist observers have reported that aircraft icing is occasionally observed while flying through high-altitude cirrus clouds at temperatures colder than -40°C . Such reports fly in the face of conventional

wisdom, however, because airframe icing under such conditions implies the accretion of liquid cloud droplets supercooled to tem-

Department of Meteorology, University of Utah, Salt Lake City, UT 84112.

peratures often well below the spontaneous freezing point of pure water (1). Because these reports have been met with incredulity, and because these scarce icing events do not lend themselves to in situ study, they have not been well documented in the literature (2). Special cloud microphysical processes seem to be involved, and an explanation for the presence of such extremely cold droplets has been suggested by recent cirrus microphysical simulations (3, 4). These numerical experiments have indicated that, below the spontaneous freezing temperature, cirrus ice crystals are produced through the homogeneous freezing of solution droplets in cirrus updrafts. Newly

formed droplets (5) are inhibited from freezing as a result of the high molalities of the aqueous solutions formed as the cloud condensation nucleus (CCN) dissolves, but with continued growth the declining freezing-point depression effects allow the drops to freeze. Figure 1 illustrates how the equilibrium particle sizes from common ammonium sulfate CCNs increase as the relative humidity rises, until at the indicated temperatures (dashed lines) they freeze homogeneously into ice crystals.

Interest in water-containing, high-altitude clouds, and cirrus cloud formation processes in general, is currently high as a result of the need to improve the treatment of the effects of cirrus clouds in climate models and better understand the possibilities of climate change from the buildup of greenhouse gases. Fortunately, a ground-based, remote-sensing tool is currently advancing our knowledge of these high clouds. The laser backscatter depolarization technique relies on the principle that spherical water drops and crystalline ice particles can be discriminated through the analysis of the polarization properties of light backscattered from clouds. Polarization diversity lidar (PDL) systems have for some time been used in this capacity for the remote sounding of cloud phase and composition (6). The simplest and most widely used method involves the transmission of a linearly polarized laser pulse and the simultaneous detection of the backscattered light in the perpendicular and parallel polarization planes, from which the linear depolarization ratio (or δ value) is derived. In an earlier report (7) Sassen *et al.* identified, using this method, cloud droplets supercooled to temperatures as low as -36°C

before they froze. Subsequent cirrus cloud observations with our apparatus have shown only slightly lower temperatures for long-lived liquid layers in compliance with the effects of spontaneous freezing, but some evidence for sporadic liquid and mixed-phase cirrus cloud regions at colder temperatures has been obtained (2, 8).

Recently, an advanced PDL system with significantly improved research capabilities was deployed during the second Project FIRE Intensive Field Observations (IFO II) campaign at Coffeyville, Kansas. This major field experiment brought together a variety of lidars, radars, passive remote sensors, and aircraft to study the basic microphysical and radiative properties of cirrus clouds. The University of Utah PDL system probed the atmosphere at high spatial (effective pulse length, 1 m) and temporal (10 Hz) resolutions at a laser wavelength of $0.532\ \mu\text{m}$. Some of the most interesting and comprehensively studied clouds occurred on 5 to 6 December 1991, during a period of moist subtropical flow when strong jet streams swept cirrus cloud systems through the project area. This flow pattern also brought from the subtropics a surge of volcanic aerosols formed from the stratospheric injections of sulfur dioxide during the mid-June 1991 Mount Pinatubo paroxysm, as evidenced by the spectacular twilight effects starting on the evening of 4 December. The unusual properties of the cirrus clouds observed on this occasion seem to be linked to an influx of volcanic aerosols into the cirrus-generating regions.

Figure 2 provides an overview of the cirrus clouds probed over a particularly interesting 80-min period on the night of 5 to 6 December. This height-versus-time display of relative returned laser power reveals two long-lasting cirrus layers. The upper cirrus layer is a tenuous cloud intermittently capped by a thin, denser layer near the tropopause (T_p) (9). The structure of the bottom layer illustrates a common cirrus-generating mechanism, in which a more or less continuous cloud base is defined by the accumulation of ice crystals generated aloft (10). The sporadically acting precipitation processes have created long, curved ice crystal fall streaks in response to the vertical wind shear in the atmosphere. Two strongly scattering cloud structures between the layers, indicative of fresh cloud-generating regions, are clearly in evidence. The cirrus-generating structure observed at 0530 (all times are UTC) at a top height of 10.0 km (all heights are above mean sea level) is just starting to inject ice into the bottom layer, while the smaller cloud observed at 0630 and 10.5 km seems to be at the beginning of its life cycle. Their detailed structures are highlighted in Fig. 3.

In the expanded returned laser power and linear depolarization ratio displays of

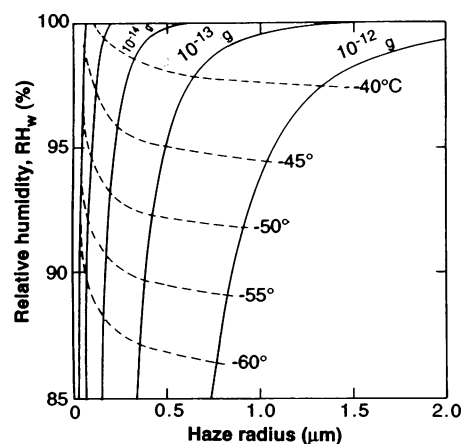


Fig. 1. Results of cirrus uncinus cloud microphysical simulations [adapted from (4)] showing the dependence of haze particle size on relative humidity with respect to water. The haze growth curves for the five ammonium sulfate CCN masses (ranging from 10^{-16} to 10^{-12} g) are likely to be interrupted by homogeneous freezing at the indicated temperatures.

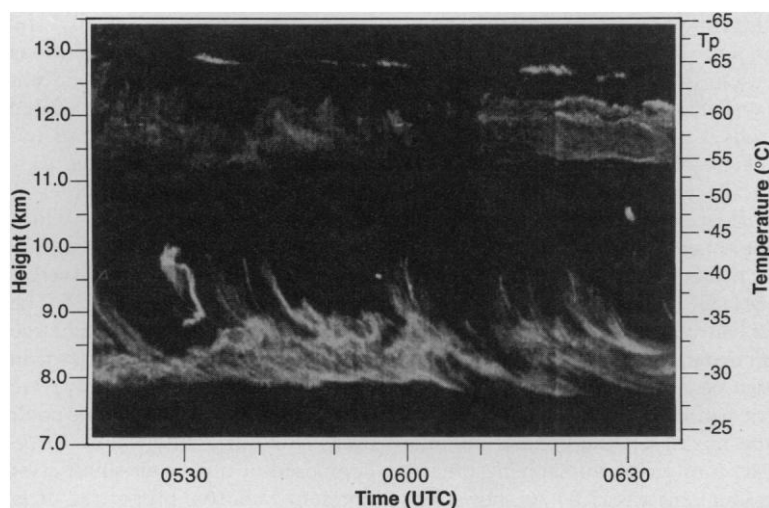


Fig. 2. Height-versus-time display of cirrus clouds probed over the indicated period on 6 December 1991, based on a gray scale (in decibels of the maximum signal shown as white) of the range-normalized returned laser power in the parallel polarization plane. Plotted resolutions are 24 m (4-point averages) in height and 6 s (60 pulses) in time. The temperature scale (valid for 0600 UTC) is based on bracketing balloon soundings launched from the remote sensor hub site.

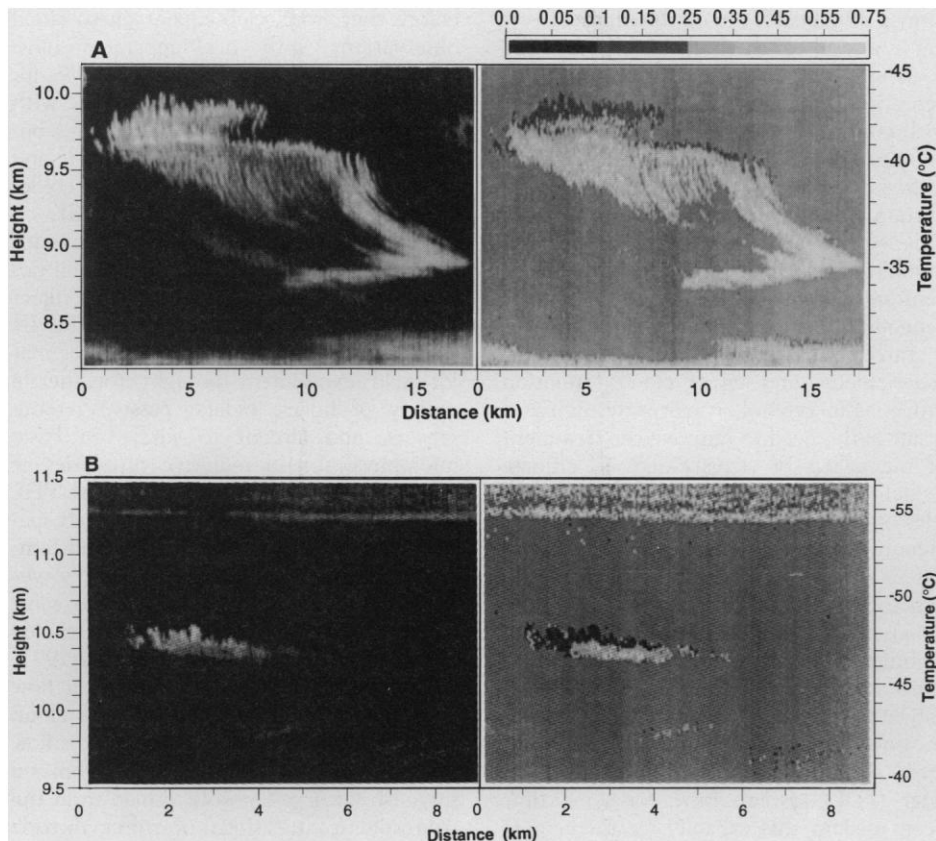


Fig. 3. Expanded views of the two strongly scattering cirrus-generating regions shown in Fig. 2 at ~0530 UTC (**A**) and 0630 UTC (**B**), in terms of returned laser power (left of each pair, as in Fig. 2) and linear depolarization ratios [right of each pair; see δ value gray scale key at the top right of (A)]. A neutral gray background is used for noise- and molecular-dominated signals in the δ displays. Plots are based on 18-m height resolutions and 1-s spatial resolutions, although distance scales derived from the measured wind speeds at the cloud top heights are shown. The actual time lengths are 400 and 200 s in (A) and (B), respectively.

Fig. 3, A and B, the time scales have been converted to distance on the basis of the wind speeds measured at the generating heights. When viewed at this scale, it is clear that these generating regions are composed of complexes of cirrus uncinus cells in various stages of development (10). The larger uncinus cell heads penetrate 100 to 300 m into cloud-free air and range from less than 100 m to nearly 300 m in diameter. Depolarization data indicate that the cell heads are composed mainly of supercooled liquid droplets (11). In contrast to the δ values of 0.35 to 0.55 (typical of cirrus crystals) present in the fall streaks and surrounding cirrus clouds, the protruding cell heads generally display minimum $\delta < 0.1$. This depolarization and returned power pattern is the signature of liquid cloud top-generating cells as is, for example, often observed in supercooled altocumulus layers. The coldest temperatures at the liquid cell tops are -43.6° and -48.7°C , respectively. Although such obvious examples of liquid-dominated cells were infrequently captured in this data set, showing them to be a transient but potentially important phenom-

enon confined to the onset of fall streak production, they provide convincing evidence for the formation of cirrus clouds through an apparently uncommon liquid-phase nucleation process over a temperature range of about -40° to -50°C .

We suggest that the presence of these extremely supercooled (that is, for pure water) droplet clouds is a consequence of the effects on cirrus clouds of volcanic aerosols. Cirrus clouds typically form at such great heights above the surface that the photochemically active stratosphere may normally be the source of activated cloud nuclei in the upper troposphere (12), but during episodes of volcanically enhanced aerosol loading, as we are now experiencing, cirrus cloud microphysical processes can be dominated by the fallout of stratospheric particles. The scenario we evoke involves the mixing of stratospheric sulfuric acid droplets into air of tropospheric origin containing ammonia gas (13). As shown by laboratory (14) and lidar volcanic aerosol research (15), the ensuing crystallization of acid droplets creates ammonium sulfate particles, which are crucial to high-altitude cirrus cloud formation via the haze particle growth-

freezing process. Although gradual mixing constantly takes place across the tropopause, rapid exchanges between the stratosphere and troposphere regularly occur owing to the effects of tropopause folding along jet streams. Large-scale cirrus cloud systems frequently form in these regions, and such clouds are likely to be affected if decaying volcanic debris is present in the lower stratosphere, as is the case here on the basis of the available FIRE data set (16). Moreover, the relatively strong backscattering observed in the liquid cells implies the presence of rather large CCNs. Because of the poor backscattering efficiencies of droplets with radii $\leq 1.0 \mu\text{m}$ at our laser wavelength (17), giant CCNs with masses of 10^{-12} g or greater are indicated at the measured temperatures (see Fig. 1).

The hypothesis that the fallout of volcanically generated aerosols will perturb the properties of "natural" cirrus clouds clearly has climatic implications. The global effects of major explosive volcanic eruptions have included noticeable decreases, estimated to be on the order of 1°C or less, in surface temperatures (18). Such effects have been attributed to the increase in planetary albedo caused by solar scattering off the enveloping veil of stratospheric acid clouds. However, the effects of impulsively perturbed cirrus cloud fields on the radiation balance of the Earth-atmosphere system could provide a significant competing or reinforcing agent for climatic adjustment in the years following major volcanic eruptions. Whichever cirrus climate trend dominates, an enhanced cooling from increasing solar scattering or an offsetting greenhouse effect caused by the absorption of terrestrial radiation, depends on the nature of the changes in cirrus cloud microphysics.

Although radiative transfer simulations have generally indicated that especially upper-tropospheric, optically thin cirrus clouds contribute to the greenhouse warming effect (19), detailed cloud microphysical-radiative simulations tailored to the haze and ice cloud alterations induced by volcanic aerosols are required to solve this problem. Assuming that larger and more abundant CCNs are introduced, one might expect cirrus clouds to be produced more readily (at lower relative humidities according to Fig. 1) and to be longer lasting (drawing from an enlarged CCN population to replenish losses from crystal precipitation). Alternatively, greatly increased CCN concentrations could lead to more gravitationally stable cirrus clouds composed of numerous small crystals with different radiative properties. It is expected that the uniquely comprehensive Project FIRE IFO II data set will help to delineate the possible connections between volcanoes, cirrus clouds, and climate perturbations.

REFERENCES AND NOTES

State-to-State Rates for the $D + H_2(v = 1, j = 1) \rightarrow HD(v', j') + H$ Reaction: Predictions and Measurements

Daniel Neuhauser,* Richard S. Judson, Donald J. Kouri,†
David E. Adelman, Neil E. Shafer, Dahv A. V. Kliner,‡
Richard N. Zare†

A fully quantal wavepacket approach to reactive scattering in which the best available H_2 potential energy surface was used enabled a comparison with experimentally determined rates for the $D + H_2(v = 1, j = 1) \rightarrow HD(v' = 0, 1, 2; j') + H$ reaction at significantly higher total energies (1.4 to 2.25 electron volts) than previously possible. The theoretical results are obtained over a sufficient range of conditions that a detailed simulation of the experiment was possible, thus making this a definitive comparison of experiment and theory. Good to excellent agreement is found for the vibrational branching ratios and for the rotational distributions within each product vibrational level. However, the calculated rotational distributions are slightly hotter than the experimentally measured ones. This small discrepancy is more marked for products for which a larger fraction of the total energy appears in translation. The most likely explanation for this behavior is that refinements are needed in the potential energy surface.

Ultimately, the test of any theory is its predictive power. In chemistry, theoretical calculations based on first principles have been applied to static properties of molecules with great success. However, theoretical calculations of dynamical properties have met with less success because of the large number of quantum mechanical (QM) scattering channels in such processes. Recent experimental advances have permitted the study of the $H + H_2$ reaction and its isotopic analogs at a level of detail previously not possible (1–9). Corresponding advances in theoretical techniques have allowed these new measurements to be compared with exact QM calculations at total energies up to 1.82 eV (10–22). Calculations for a range of total energies have been restricted to energies below 1.35 eV (10, 12–14, 18), whereas results for reactions in which the H_2 was vibrationally excited have been obtained only for total energies ranging from 0.82 to 1.35 eV (18) and for 1.82 eV (16, 21). The QM calculations (10–14, 18, 20) agree well with integral cross section measurements (1–3, 8) in the total energy regime below 1.5 eV.

Significant differences have been found between experiment (5, 8) and theory (16, 21) at the higher total energy of 1.82 eV. Two factors may influence this comparison: (i) the theoretical calculations did not fully simulate the experimental conditions; and (ii) the experimental results may have been impaired to some extent by space-charge effects caused by ion production in the use of DBr as a photolytic source of fast D atoms. Consequently, it was not possible to determine whether the differences between experiment and theory were caused by experimental error, the incomplete simulation of the experiment, the potential energy surface (PES), or the accuracy of the QM calculations. The theoretical predictions were essentially unchanged in a subsequent more accurate study (22); however, these calculations also did not include a full simulation of the experimental conditions. At such high energies, it may well be that the PES is less reliable for these comparisons with experiment because regions of greater anisotropy and anharmonicity can be sampled, that is, experiments at lower energies may be less sensitive to inaccuracies in the PES.

Existing noniterative time-independent quantal scattering methods rapidly become computationally intensive at higher total energies because of the increase in the number of quantum channels (10–22). We report here theoretical results obtained with a newly developed wavepacket approach (21, 23–26) to exact scattering dynamics that extends the predictive power of theory to higher energies and more complex scattering systems; consequently, a full simulation of the experimental conditions was feasible. We also report new state-to-state integral cross section measurements of the $D + H_2(v$

D. Neuhauser, James Franck Institute, University of Chicago, Chicago, IL 60637.

R. S. Judson, Sandia National Laboratory, Center for Computational Engineering, Livermore, CA 94551–0969.

D. J. Kouri, Department of Chemistry and Department of Physics, University of Houston, Houston, TX 77204–5641.

D. E. Adelman, N. E. Shafer, D. A. V. Kliner, R. N. Zare, Department of Chemistry, Stanford University, Stanford, CA 94305–5080.

*Present address: Department of Chemistry, University of California, Los Angeles, CA 90024.

†To whom correspondence should be addressed.

‡Present address: Department of Chemistry, University of Minnesota, Minneapolis, MN 55455.

- B. J. Mason, *The Physics of Clouds* (Clarendon, Oxford, 1971), p. 174.
- K. Sassen, D. O'C. Starr, T. Uttal, *J. Atmos. Sci.* **46**, 371 (1989).
- A. J. Heymsfield and R. M. Sabin, *ibid.*, p. 2252.
- K. Sassen and G. C. Dodd, *ibid.*, p. 3005.
- It is more accurate to refer to these droplets as haze particles, because at such low temperatures they probably remain in environmental equilibrium below their critical radii until freezing.
- K. Sassen, *Bull. Am. Meteorol. Soc.* **72**, 1848 (1991).
- _____, K. N. Liou, S. Kinne, M. Griffin, *Science* **227**, 411 (1985).
- We have regularly collected polarization ruby lidar data from cirrus clouds since 1987 in support of the Extended Time Observations component of Project FIRE.
- Local Project FIRE radiosonde data have provided atmospheric temperature and wind information, based on the use of a time-weighted average of high-resolution (~40 m) data obtained at 0030 and 0905 UTC on 6 December 1991.
- K. Sassen, C. J. Grund, J. D. Spinhirne, M. M. Hardesty, J. M. Alvarez, *Mon. Weather Rev.* **118**, 2288 (1990).
- The question of the ambiguity in PDL cloud phase discrimination deserves discussion. Near-zero δ values can be produced by homogeneous spheres, plate crystals large enough ($\geq 250 \mu\text{m}$ in diameter) to orient horizontally, and aspherical particles smaller than the incident wavelength (air molecules). The rapidly rising turrets (note the absence of wind shear effects) in Fig. 3 must contain relatively small particles, certainly too small to orient uniformly. On the other hand, laboratory experiments with artificially "seeded" supercooled clouds demonstrate that minute frozen droplets rapidly grow the facets needed to produce optical depolarization [K. Sassen and K. N. Liou, *J. Atmos. Sci.* **36**, 852 (1979)]. Lidar observations of aircraft condensation trails and glaciating clouds (7) show the same rapid transition in δ as ice crystals form. Although some ice nucleation probably took place in the cell heads, we conclude that liquid droplet backscattering predominated.
- Cloud-forming nuclei derived from at or near the Earth's surface are deficient at cirrus altitudes because of sedimentation. Lidar studies of cirrus clouds that straddle high tropopause have revealed unusual cloud properties that probably reflect the effects of stratospheric-derived CCNs [K. Sassen, *Appl. Opt.* **30**, 3421 (1991)].
- It is also possible that the sulfuric acid droplets could freeze directly into ice crystals during growth from tropospheric water vapor.
- K. Sassen *et al.*, *Appl. Opt.* **28**, 3024 (1989).
- K. Sassen and J. D. Horel, *J. Atmos. Sci.* **47**, 2881 (1990).
- Preliminary supporting remote and in situ data from Project FIRE have shown directly the mixing of stratospheric ozone and volcanic aerosols into the cirrus cloud altitude during this period.
- For example, Mie scattering theory simulations reveal that a water droplet of radius $1.3 \mu\text{m}$ backscatters ~70 times as much light at the $0.532\text{-}\mu\text{m}$ wavelength as a $0.7\text{-}\mu\text{m}$ droplet, suggesting that, if only submicrometer-sized droplets were present, these unusual cloud features might have gone unnoticed.
- P. E. Ardanuy and H. L. Kyle, *J. Clim. Appl. Meteorol.* **25**, 505 (1986).
- K. N. Liou, *Mon. Weather Rev.* **114**, 1167 (1986).
- Support for our FIRE IFO research has come from National Science Foundation grant ATM-8914348 and National Aeronautics and Space Administration grant NAG-1-868 and for PDL development from Department of Energy grant DE-FG02ER1059 from the Atmospheric Radiation Measurement program. I thank M. T. Davies and B. S. Cho for their contributions, and various FIRE coinvestigators for making available their preliminary data.

17 March 1992; accepted 1 June 1992